博士論文

Comparison of physical image qualities and artifact indices for head computed tomography in the axial and helical scan modes

アキシャルスキャンモードとヘリカルスキャンモードにおける頭部 computed tomography の物理的な画質とアーチファクト指標の比較

氏　　　　名　藤村　一郎
主任指導教員　市川　勝弘　教授

提出年月日　　令和２年７月 16 日

Contents

Abstract

Head computed tomography (CT) can be acquired by using both the axial and helical scan modes (AS and HS, respectively) that implemented in all of the clinical scanners. The equivalency between these modes has been clinically demonstrated in various previous studies. This study aimed to validate the clinically demonstrated equivalency of the AS and HS for head computed tomography (CT) using physical image quality measures and artifact indices (AIs).

Two 64-row multi-detector row CT systems (CT-A and CT-B) were used for comparing AS and HSs with detector rows of 64 and 32. The modulation transfer function (MTF), noise power spectrum (NPS), and slice sensitivity profile were measured using a CT dose index corresponding to clinical use. The system performance function (SPF) was calculated as MTF^2/NPS. The AI of streak artifacts in the skull base was measured using an image obtained of a head phantom, while the AI of motion artifacts was measured from images obtained during the head phantom was in motion.

For CT-A, the 50%MTFs were 7 to 9 % higher in the HS than the AS, and the higher MTFs of HS associated NPS increases. For CT-B, the MTFs and NPSs were almost

equivalent between the AS and HS, respectively. Consequently, the SPFs of AS and HS were nearly identical for both CT systems. For both CT systems, the skull base AI did not differ significantly between AS and HS, while the motion AIs of HS were significantly better than of AS. The superior motion AI in the HS indicated the effectiveness of HS on moving patients.

List of Tables

List of Figures

Fig. 6 Measured slice sensitivity profiles (SSPs)

Fig. 7 Skull base AI values measured from images obtained by scanning a head phantom composed of a dry human skull bone shown in Fig. 1. ns: not significant

Fig. 8 Representative skull base images generated using the (a) AS, (b) HS-64, and (c) HS-32 for the CT-A and (d) AS, (e) HS-64, and (f) HS-32 for the CT-B

Fig. 9 Motion AI values measured on scanned images of the PH-34 phantom with a rolling motion. *: P <0.05, ns: not significant

Fig. 10 Representative images of motion artifacts generated using the (a) AS, (b) HS-64, and (c) HS-32 for the CT-A and (d) AS, (e) HS-64, and (f) HS-32 for the CT-B

List of Abbreviations

AS	Axial scan mode
HS	Helical scan mode
CT	Computed tomography
MDCT	Multi-detector row CT
$CTDI_w$	Weighted CT dose index
SSP	Slice Sensitivity profile
SD	Standard deviation
CNR	Contrast-to-noise ratio
MTF	Modulation transfer function
NPS	Noise power spectrum
AI	Artifact index
$CTDI_{vol}$	Volume CT dose index
FBP	Filter back projection
DFOV	Display fields of view
1D	One dimensional
2D	Two dimensional
HU	Hounsfield unit

NEQ	Noise equivalent quanta
SPF	System performance function
ROI	Region of interest
FWHM	Full width at half maximum
FWTM	Full width at tenth maximum

Acknowledgements

There are many people I wish to thank for their kind support and mentorship during my Ph.D studies. First and foremost, I would like to thank my supervisor Dr. Katsuhiro Ichikawa for his encouragement and guidance. I have learned from him not only how to do a research but also how to be a research scientist. I would also like to thank my other laboratory members, Takanori Hara Ph.D, Eiji Nishimaru Ph.D, Kazuya Ohashi Ph.D, Atsushi Urikura Ph.D, and Takeshi Inoue MS for their helpful comments and supports throughout this project. This work would not have been possible without the help and support from Keiji Sakashita MS at Rinku general medical center, Takeshi Mito RT at Minoh city hospital, Yuji Miyazaki MS at Wakayama medical university hospital, and the people involved Butsuryo College of Osaka.

1 Introduction

Head computed tomography (CT) can be acquired by using both the axial and helical scan modes (AS and HS, respectively) that implemented in all of the clinical scanners. The AS and HS have been evaluated as clinically equivalent, for the head computed tomography (CT) scans using multi-detector row CT (MDCT) systems with 64 or more rows [1-4]. Despite this general equivalency, reports have described three discrepancies in subjective evaluations. One such discrepancy involves the advantage of HS for the quality of multiplanar reformation images [5-7]. Another discrepancy involves artifacts in the posterior fossa, which were significantly worse in the AS relative to the HS for a 64-row MDCT system [1]. Although thin detector collimations can reduce artifacts [8], a previous report did not provide the detector configuration for the AS. The other discrepancy involves visualization of the cerebral cortex adjacent to the calvarium cephalad, which was evaluated lower in HS than in AS on a 128-row MDCT system [2]. This discrepancy appears to have resulted from a difference in the slice thickness and/or beam hardening correction. However, the slice sensitivity profiles (SSPs) and details of beam hardening correction were not previously reported. In the previous studies comparing AS and HS, the quantitative evaluations were limited to standard deviations (SD) and contrast-to-noise ratios (CNR). To the best of our knowledge, no studies have compared the AS and HS for head CT in terms of physical image qualities such as the modulation transfer function (MTF), noise power spectrum (NPS), and SSP. Therefore, this study aimed to use multiple parameters, including the MTF, NPS, and SSP, to validate the equivalency between the AS and HS for head CT. Artifact indices (AIs) of beam hardening streak artifacts in the skull base, with and without head motion, were also compared.

2 Methods and Materials

2.1 Scan and reconstruction parameters

Two 64-row MDCT systems were used. One CT system (CT-A) had detector rows of 0.5 mm × 64, and the other system (CT-B) had detector rows of 0.625 mm × 64. **Table 1** shows scan and reconstruction parameters of AS and HS for CT-A and CT-B, used in this study. These parameters corresponded to ones for clinical use. The detector configurations for AS were 4 mm × 4 for CT-A and 5 mm × 4 for CT-B. The detector configurations for HS were the 32-row (HS-32) and 64-row modes (HS-64), which were 0.5 mm × 32 and 0.5 mm × 64, respectively, for CT-A and 0.625 mm × 32 and 0.625 mm × 64, respectively, for CT-B. The tube currents were adjusted such that the weighted CT dose index ($CTDI_w$) for AS and the volume CT dose index ($CTDI_{vol}$) for

HS were approximately 60 mGy. The CT images were reconstructed using nominal slice thicknesses of 4 and 5 mm for CT-A and CT-B, respectively. The filter back projection (FBP) was used as reconstruction algorithms for both CT systems. We did not use

higher pitch factors (e.g., ≥0.8) because these were not recommended by the manufacturers [3], and because the HS scan durations are sufficiently short (~7 s for HS-64) in most clinical situations based on 64-row MDCT systems.

Table 1 Scan and reconstruction parameters used in this study

	CT-A			CT-B		
Scan mode	AS	HS	HS	AS	HS	HS
Axial configuration (mm)	4 x 4	32 x 0.5	64 x 0.5	4 x 5	32 x 0.625	64 x 0.625
Peak voltage (kVp)	120	120	120	120	120	120
Tube current (mA)	260	170	190	300	160	160
CTDI vol. (mGy)	59.2	59.6	60.1	59.1	60.4	59.7
Rotation time (s)	1.0	1.0	1.0	1.0	1.0	1.0
Pitch factor	—	0.656	0.641	—	0.531	0.516
Reconstruction slice thickness (mm)	4	4	4	5	5	5
Reconstruction kernel	FC21	FC21	FC21	Standard	Standard	Standard

2.2 Modulation transfer function

MTFs were measured using a handmade metal wire phantom constructed with a metal (Cu) wire with a diameter of 0.15 mm and a cylindrical acrylic case (diameter = 50 mm). The case was filled with water. The small phantom size (50 mm) was used to improve the measurement accuracy of MTF by reducing image noise, which was valid because it is known that FBPs yield CT images with linear properties independent of detector dose. This phantom was carefully positioned such that its central axis was exactly parallel to the rotation axis of the CT system. Next, the position of the wire was set with a 10-mm offset in the y-direction to avoid a specific (typically, somewhat lower) MTF induced by the coaxial position of the central axis of the phantom with the rotation axis of the CT system [9]. CT images were reconstructed using minimally available display fields of view (DFOVs) of 50 mm for CT-A and 100 mm for CT-B to precisely detect the point spread functions from the thin wire. A 256-pixel × 256-pixel sub-image around the wire was analyzed using a 2D fast Fourier transform. Then, the radial averaging technique, in which the fx and fy frequencies in two dimensional (2D) data were collapsed to a one dimensional (1D) radial frequency fr (distance from center point in frequency coordinate), was applied to generate the final 1D MTF [9-11].

2.3 Noise power spectrum

The NPS was measured using a water phantom (diameter = 20 cm) with an absorption similar to that of the adult head [12]. Uniform noise images were obtained by scanning the water phantom, and a central 256-pixel × 256-pixel region on each image was processed using an established method with the 2D fast Fourier transform [13-15]. The CT number in Hounsfield units (HU) is used to calculate the NPS. 2D NPS measurements were converted to a 1D NPS using the radial averaging technique mentioned in the method subsection of MTF. The 1D data were binned into 40 frequency bins to mitigate the data fluctuations in NPS. To reduce the variability of the NPS results, we considered the average value of at least 80 slices obtained from four scans of the phantom. Although this phantom has a homogeneous content of water, the influences of skull attenuation correction on the images for both CT systems were slight and negligible.

2.4 System performance function

The noise equivalent quanta (NEQ) is the effective number of photons acquired by the detector; for CT, the NEQ, as a function of the spatial frequency u, can be calculated as:

$$NEQ(u) = u \cdot MTF^2(u) / NPS_A(u), \tag{1}$$

where $NPS_A(u)$ is another version of the NPS calculated using the linear attenuation coefficient μ instead of the CT number in HU [16]. For the purpose of this study, the absolute NEQ-derived value was not required; accordingly, the $NPS(u)$ calculated using the CT number in HU was used for relative evaluations of imaging performance. Moreover, focusing on the image quality term $MTF^2(u)/NPS(u)$ in equation (1), we defined this measure as a system performance function (SPF) as follows:

$$SPF^2(u) = MTF^2(u) / NPS(u) \tag{2}$$

This calculation is based on the principle of the pre-whitening theorem [17]; thus SPF is independent of filter kernel because the MTF^2 term has the same spatial frequency dependence as NPS. Thus, by using the SPF, the image qualities can be compared between systems with different MTFs.

2.5 Slice sensitivity profile

The SSP was measured using a bead phantom [11, 18]. This phantom, which contains a small (diameter: 0.2 mm) bead of lead, was included in the JCT II phantom set (Kyoto Kagaku Co., Kyoto, Japan) provided for quality control. The same z-collimations and reconstruction slice thicknesses as those of other measurements were used. CT images were reconstructed with a DFOV of 100 mm and increments in table position of 0.2 mm. The average value of a region of interest (ROI) placed circumferentially around the bead was measured in each image, and the values with respect to the table position were plotted after normalization based on the peak ROI value. The full width at half maximum (FWHM), which is usually defined as the effective slice thickness, and full width at tenth maximum (FWTM) values were obtained from the measured SSP.

2.6 Artifacts in the skull base

Artifacts in the skull base were measured from images obtained by scanning a head phantom composed of a dry human skull bone and an acrylic case resembling the outline of a head (PH-34; Kyoto Kagaku Co., Ltd, Kyoto, Japan), as shown in **Fig. 1(a)**. The internal space in the phantom was filled with water. As previously reported [19], the AI was calculated as:

$$AI = \sqrt{SD_a^{\ 2} - SD_b^{\ 2}}\ , \tag{3}$$

where SD_a is the average SD of circular ROIs placed at four locations in the skull base and SD_b is the average SD measured at the supratentorial region where artifacts usually do not occur **{Fig. 1(b) and 1(c)}**. This AI calculation is based on a well-known principle of noise addition [20]. All ROI sizes were set to 500 mm^2. We repeated the phantom scans 10 times and compared the average AI results from the AS, HS-64, and HS-32.

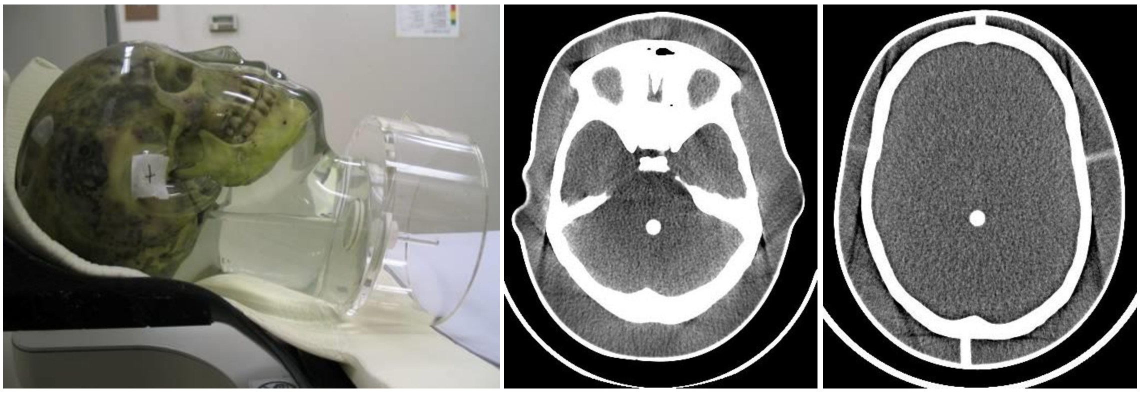

(a) (b) (c)

Fig. 1 (a) A photo of the head phantom. (b and c) Representative CT images used to measure artifact index (AI) of skull base. The average standard deviation (SD) was calculated from four regions of interest (ROIs, dotted line circles) in each of (b) the skull base image with artifacts and (c) supratentorial image without artifacts. The artifact index (AI) was calculated from these two average SD values

2.7 Motion artifact

Motion artifacts were measured on scanned images of the above mentioned head phantom with motion. As shown in **Fig. 2,** the phantom was axially rolled during the scan using lateral force delivered via a self-made mechanism comprising a 20-ml syringe (SS-20ESZ; Terumo Corporation, Tokyo, Japan) and a power injector (Dual Shot GX7; Nemoto Kyorindo Co., Ltd., Tokyo, Japan) with a dedicated syringe. Water in the dedicated syringe was injected into the 20-ml syringe to push the plunger out. The plunger speed was set to 10 mm/s by adjusting the injection speed. The AI was measured at four locations, as described for the measurement of skull base artifacts, and the same SD_b values were reused in the calculation. As described for the skull base artifacts, the phantom scans were repeated 10 times. The average AI results were compared between the AS, HS-64, and HS-32.

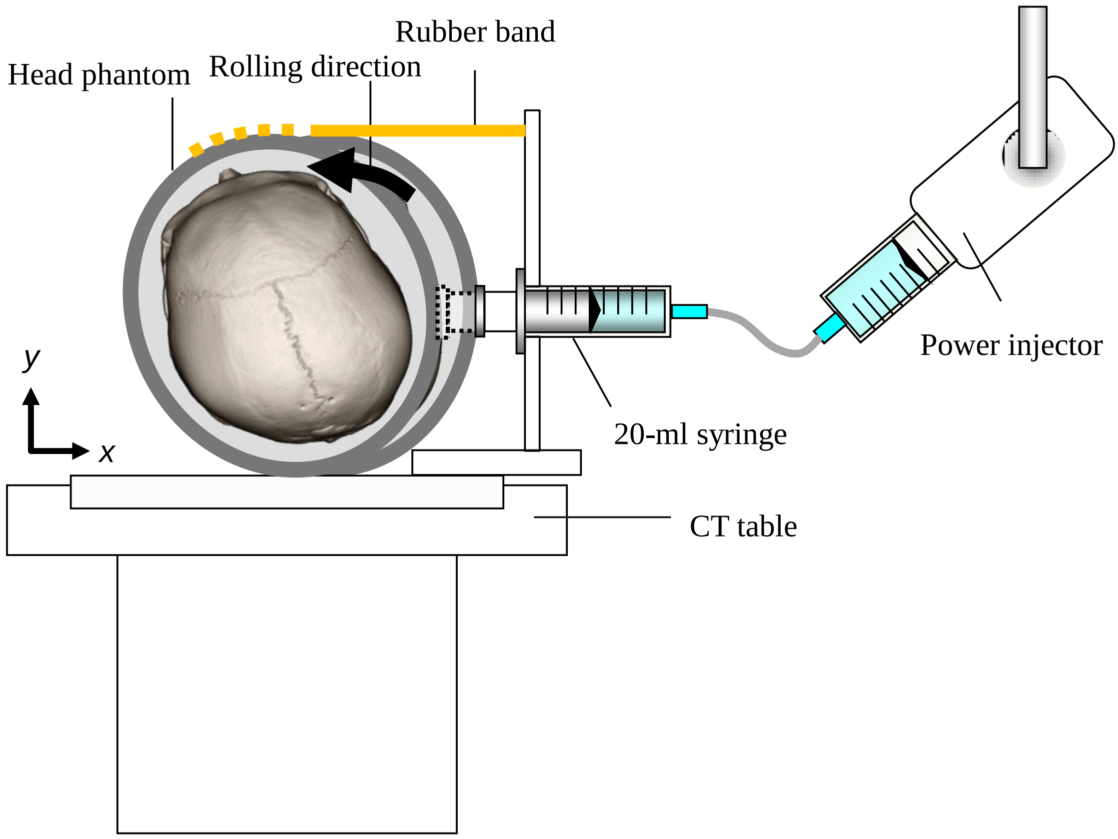

Fig. 2 Schematic of the experimental configuration used to measure motion artifacts. The phantom was rolled axially during the scan by lateral force delivered via a self-made mechanism. The speed of the plunger used to push the phantom was set to 10 mm/s

2.8 Statistical evaluation

The AI results were statistically compared between AS, HS-64, and HS-32 for each of the skull base and the motion using SPSS software, version 17.0 (IBM, Tokyo, Japan). A Wilcoxon signed-rank test was applied to the data. The Bonferroni correction was required to counteract the problem of multiple comparisons using three samples (AS, HS-64, and HS-32). Differences with p values < 0.05 were considered statistically significant.

3 Results

3.1 Modulation transfer function

Figure 3 presents the MTF results. The reproducibility of our MTF measurements was sufficiently high because the contrast-to-noise ratio of Cu wire images were very high (> 400); accordingly, error bars are not indicated on the MTF results. CT-A yielded slightly higher MTFs in the HS than in the AS, whereas the MTFs in the HS-64 and HS-32 were very similar. The 50%MTF and 10%MTF (50%MTF/10%MTF) for AS, HS-64, and HS-32 were 0.40/0.74, 0.43/0.76, and 0.44/0.77 cycles/mm, respectively. The CT-B yielded almost identical MTFs in the AS and HS.

3.2 Noise power spectrum

Figure 4 depicts the resultant NPSs. The CT-A yielded slightly higher NPSs in the HS than in the AS.

3.3 System performance function

Figure 5 presents the calculated SPFs. The SPFs did not differ noticeably between AS, HS-64, and HS-32 on either the CT-A or CTB.

3.4 Slice sensitivity profile

Figure 6 shows SSPs**. Table 2** presents the corresponding FWHMs and FWTMs of the SSPs and relative values compared to each value of AS. The two CT systems had almost identical effective slice thicknesses (FWHMs) in the AS and HS. However, the FWTMs in both HS-64 and HS-32 were increased relative to the AS by 7% on the CT-A and by 21% on the CT-B.

3.5 Artifacts in the skull base

Figure 7 presents the AI data measured from the skull base images obtained by scanning the PH-34 head phantom composed of dry human skull bone. The AIs of the

AS, HS-64, and HS-32 did not differ significantly for either CT system. **Figure 8** depicts representative CT images of the skull base. Corresponding to the AI results, no notable differences were observed.

3.6 Motion artifact

Figure 9 presents the results of the motion AI measured on scanned images of the head phantom with the rolling motion. Notably, the AS was significantly inferior to the HS on both the CT-A and CTB ($p < 0.05$). Consistent with the results, severe artifacts are visible on AS images, as shown in **Fig. 10**. The motion artifacts were well suppressed on images obtained using the HS-64 and HS-32.

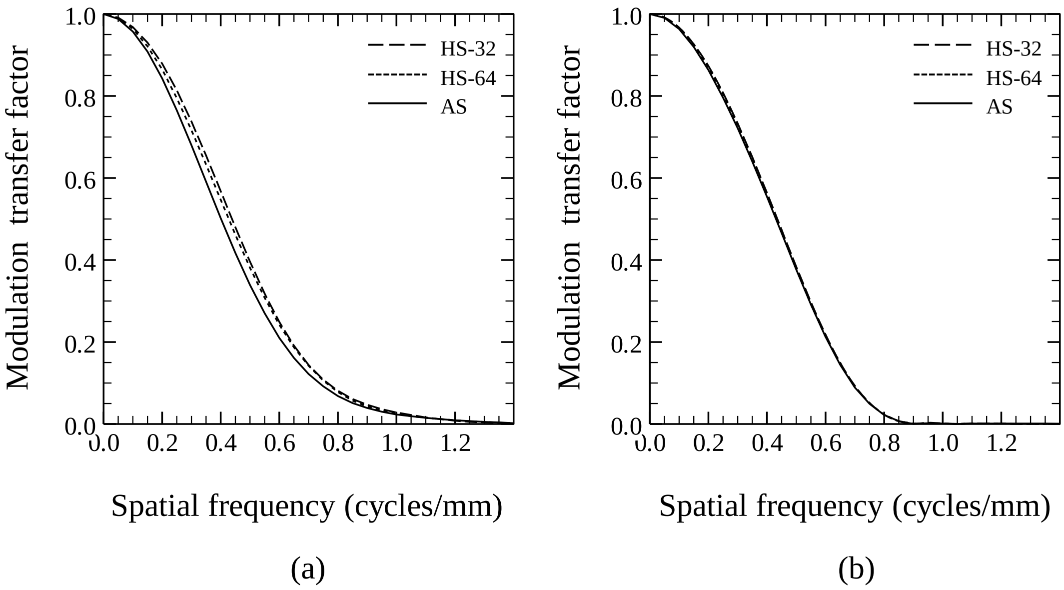

Fig. 3 Measured modulation transfer functions (MTFs)

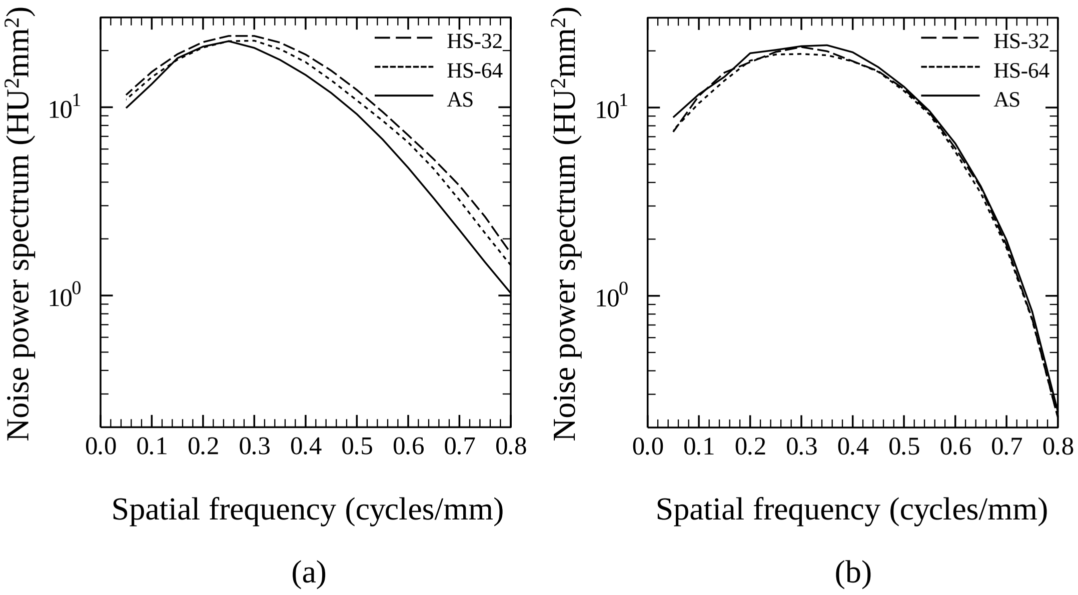

Fig. 4 Measured noise power spectra (NPSs)

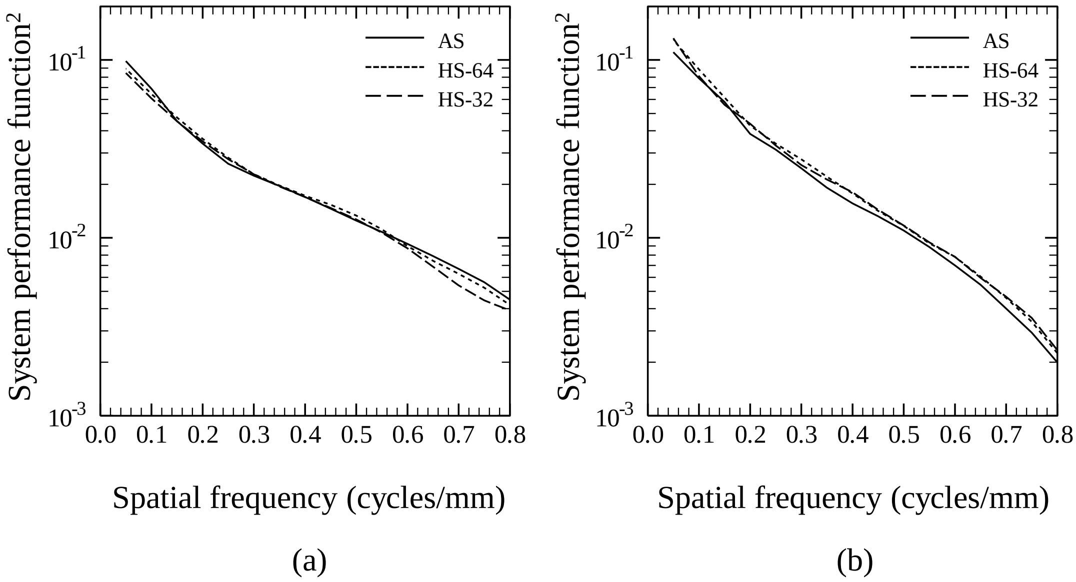

Fig. 5 System performance functions (SPFs) calculated by dividing MTF^2 by NPS

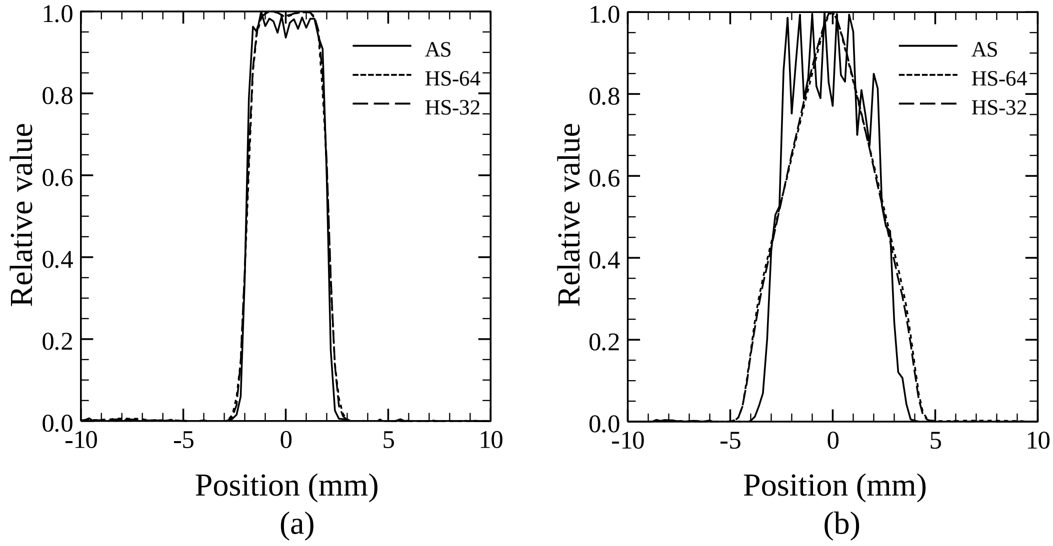

Fig. 6 Measured slice sensitivity profiles (SSPs)

Table 2 Full width of half maximum (FWHM) and Full width of tenth maximum (FWTM) of slice sensitivity profiles for AS and HS. The values in parentheses represent relative values compared to each value of AS

	CT-A		CT-B	
	FWHM (mm)	FWTM (mm)	FWHM (mm)	FWTM (mm)
AS	4.0 (1.00)	4.5 (1.00)	5.3 (1.00)	6.8 (1.00)
HS-64	4.0 (1.00)	4.8 (1.07)	5.3 (1.00)	8.2 (1.21)
HS-32	4.0 (1.00)	4.8 (1.07)	5.2 (0.98)	8.2 (1.21)

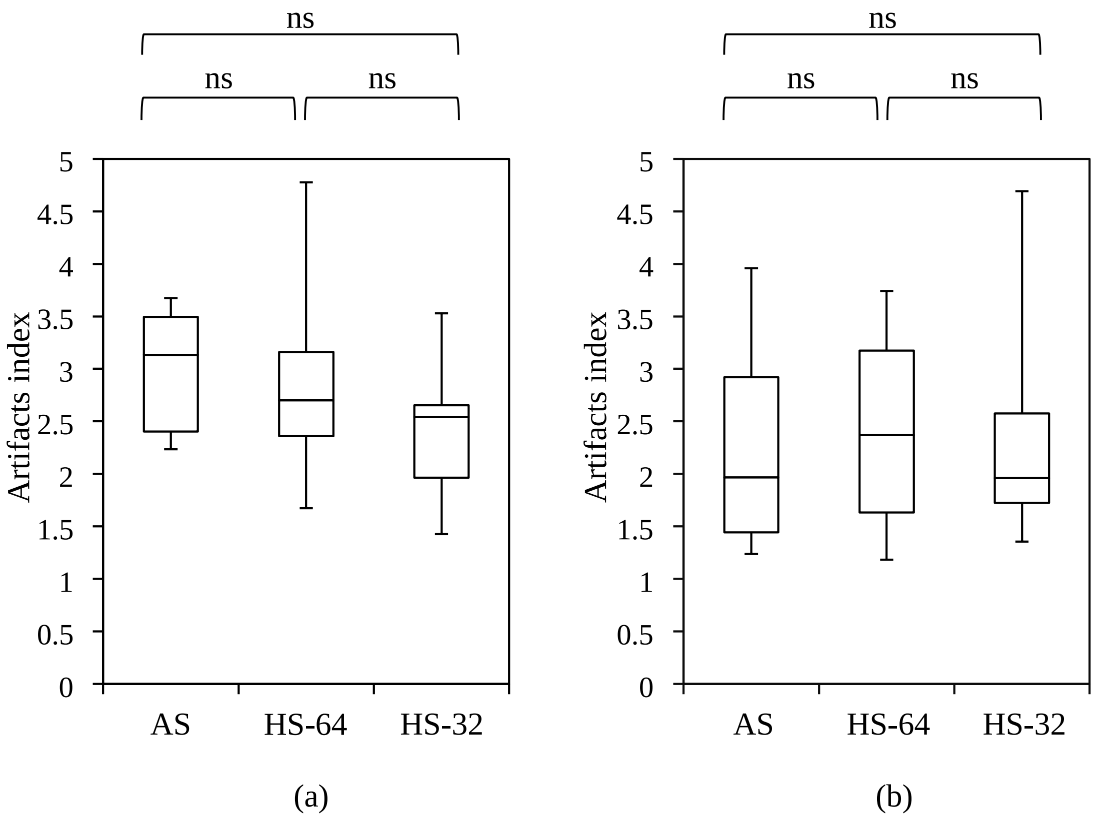

Fig. 7 Skull base AI values measured from images obtained by scanning a head phantom composed of a dry human skull bone shown in Fig. 1. ns: not significant

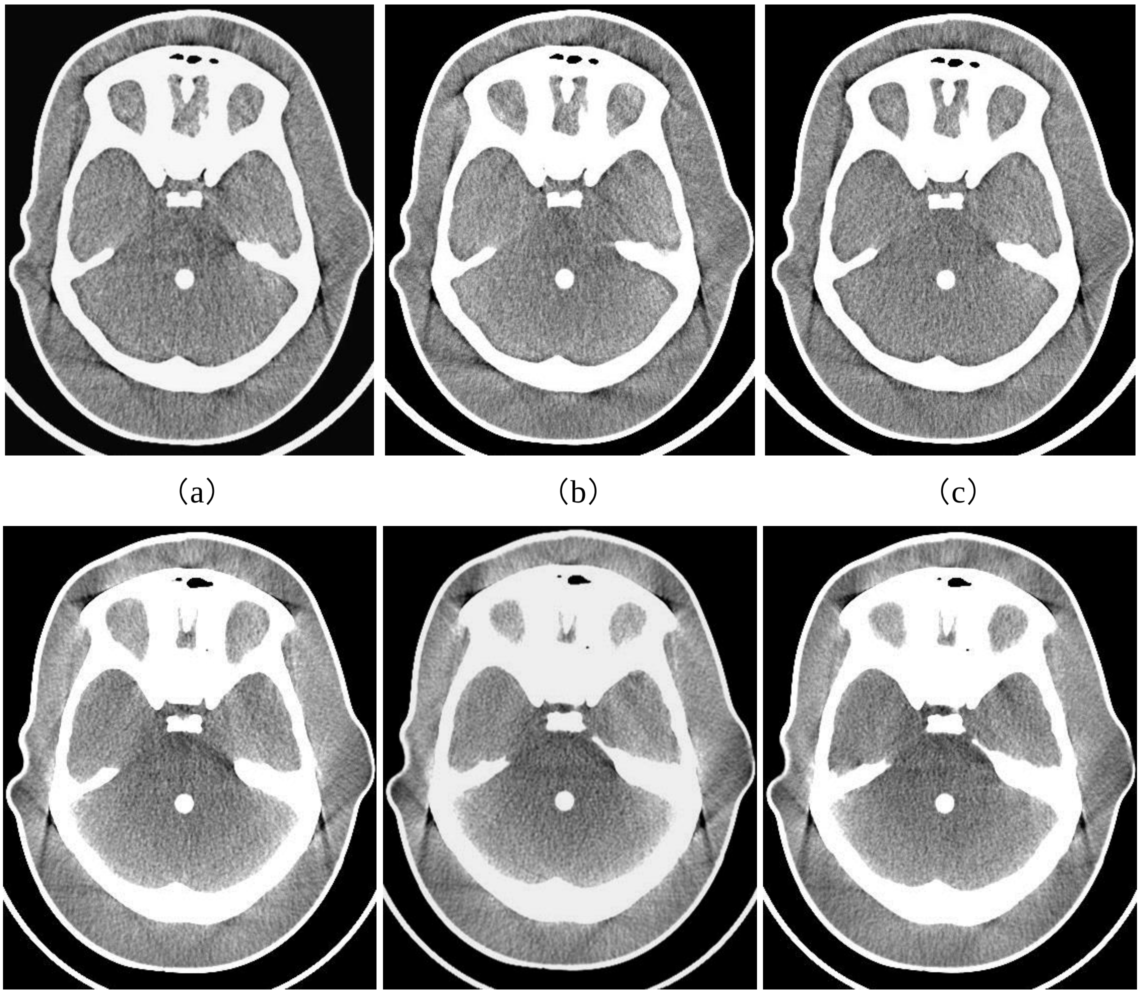

(a) (b) (c)

(d) (e) (f)

Fig. 8 Representative skull base images generated using the (a) AS, (b) HS-64, and (c) HS-32 for the CT-A and (d) AS, (e) HS-64, and (f) HS-32 for the CT-B

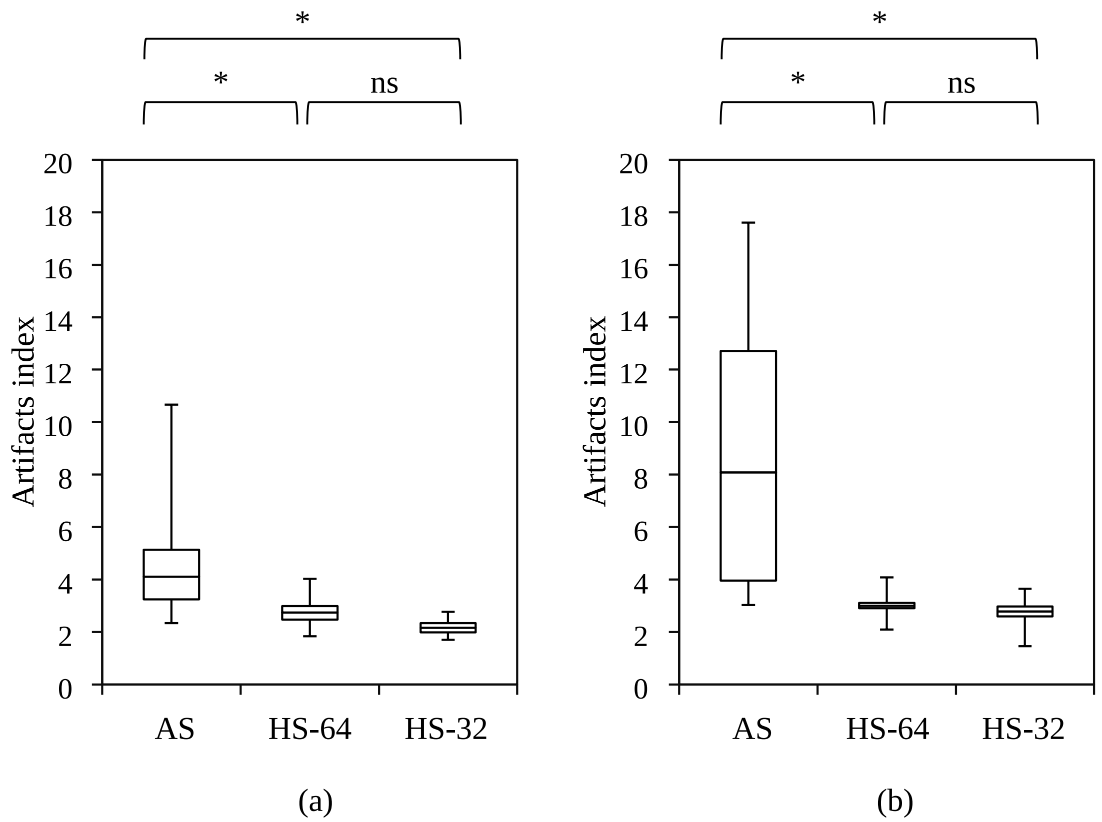

Fig. 9 Motion AI values measured on scanned images of the PH-34 phantom with a rolling motion. *: P <0.05, ns: not significant

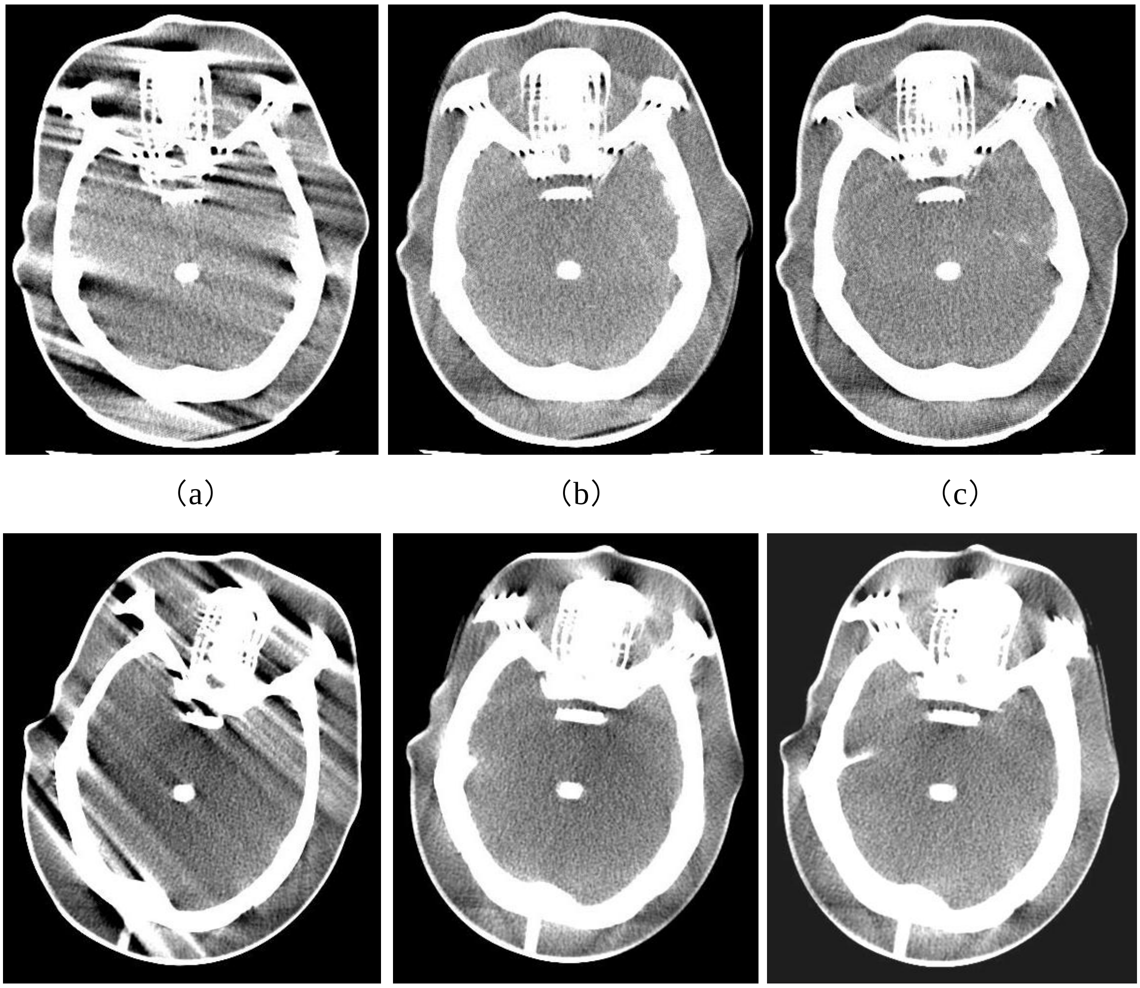

(a) (b) (c)

(d) (e) (f)

Fig. 10 Representative images of motion artifacts generated using the (a) AS, (b) HS-64, and (c) HS-32 for the CT-A and (d) AS, (e) HS-64, and (f) HS-32 for the CT-B

4 Discussion

This study measured MTF, NPS, and SSP as indices of in-plane spatial resolution, noise, and z-directional spatial frequency (slice thickness), respectively for the AS and HS. For the CT-A scanner, the MTFs were slightly higher in the HS than in the AS, and the NPSs were also slightly higher in the HS, especially at middle to high frequencies. the NPS increases in the HS were attributable to the enhanced noise caused by the higher MTFs of HS because the SPF results of HS and AS were nearly identical, meaning that the difference in MTFs was canceled out by the calculation of SPF. Accordingly, the SPF results from the CT-A revealed the equivalent imaging performances of the AS and HS. On the CTB, the MTFs of the HS and AS were almost identical, and the NPSs were also nearly equivalent. Consequently, the SPFs were equivalent between the AS and HS. These results demonstrate that the imaging performances of both the HS and AS were nearly equivalent under the same CTDI, indicating that the HS does not cause any loss of dose efficiency during the acquisition and reconstruction processes.

We did not perform CNR measurements generally using a low-contrast phantom because we determined preliminarily that the MTFs of the AS and HS differed when using the CT-A; basically, the CNR is not appropriate for comparing systems with different MTFs [21]. Two previous studies based on 64-row CT systems presented significant differences of CNR, where CNR of AS was higher than that of HS in one report [1], and, in contrast, CNR of AS was lower than that of HS in the other report [2]. However, it remains unclear whether the AS and HS differed substantially because the MTFs were not measured in these studies.

The skull base AI results did not differ significantly between the AS and HS when either the CT-A or CT-B was used, and the observed phantom images of the skull base were consistent with the AI results (**Fig. 8**). These findings indicate that the reconstruction algorithms of the CT-A and CT-B were sufficiently sophisticated and could reduce the artifacts and equalize the degrees of artifact between the AS and HS. Although the appearances of the brain peripheral regions adjacent to the skull bone differed between the images produced by the CT-A and CT-B, we considered this variation to be within the range of image characteristics usually accepted by most radiologists. Though, in Fig. 8, some edge artifacts were observed in thick spaces between the skull bone and the outer perspex, we presumed that these artifacts would disappear in actual images of human heads. It is possible that these artifacts were caused by data correction processes (e.g. skull attenuation correction) for head protocols.

We note that the motion artifacts caused by the AS were effectively suppressed by the HS on both CT systems. The AI values in the AS were significantly higher than those in the HS. The pitch factors used for HS were quite low on both CT systems (~0.65 for CT-A and ~0.52 for CT-B). The effective temporal resolutions of such low pitch factors may be inferior to those of AS even under the same rotation speed [22]. Thus, it was suggested that the effective temporal resolutions of HS were somewhat inferior to that of AS for both systems. Nevertheless, fewer motion artifacts were observed on HS images than on AS images.

We presume that this suppression effect was attributable to the implementation of projection data interpolation in the helical interpolated reconstructions performed using both CT systems. We hypothesize that the helical interpolation process acted as a time domain interpolation process wherein which the projection data inconsistencies caused by patient motion were smoothed and suppressed. This effect must be imperfect because the interpolation was not designed to reduce motion artifact. Moreover, there are various motion patterns in clinical situations. Accordingly, we presume that the reduction of artifacts depends strongly on the degree of motion and the motion pattern. In fact, some streaking, multiple bone edges, and image blurring can be observed in the HS image in **Fig. 10**. To our knowledge, this motion suppression effect of HS has not previously been reported clinically or quantitatively, although some impressions regarding the motion artifact suppressing effect of HS have been discussed within our community of

Japanese radiological technologists. In this study, our ability to demonstrate this effect quantitatively using an AI measured using a moving head phantom is notable.

This study had some limitations. First, only two CT systems were used, and therefore different systems may not be able to achieve the image quality equivalency between AS and HS presented herein. Second, we also used only one type of head phantom. Again, the equivalency between AS and HS demonstrated in this study may not be achievable with different phantoms, given the individual differences in the bone structure and density distribution of the human head. Third, we examined only one pattern of rolling motion. Further investigations of different motion patterns corresponding to clinical situations are needed to characterize the motion artifact reducing effect of the HS.

5 Conclusion

Consistent with previous reports of clinical similarities between the AS and HS, we observed nearly identical physical image qualities obtained using these two modes. Although we did not observe significant differences in the skull base artifacts, the motion artifacts were reduced significantly with the HS relative to the AS on both CT systems, suggesting that HS is recommendable for patients who find it difficult to maintain a static posture.

References

1. Abdeen N, Chakraborty S, Nguyen T, dos Santos MP, Donaldson M, Heddon G, Schwarz BA. Comparison of image quality and lens dose in helical and sequentially acquired head CT. Clin Radiol. 2010 Nov; 65(11): 868-873.
2. Davis AJ, Ozsvath J, Vega E, Babb JS, Hagiwara M, George A. Continuous versus sequential acquisition head computed tomography image quality comparative study. J Comput Assist Tomogr. Nov-Dec 2015; 39(6): 876-881.
3. Adult Routine Head CT Protocols Version 2.0; 2016. A web document of the Alliance for Quality Computed Tomography (AQCT) of American Association of Physicists in Medicine (AAPM). https://www.aapm.org/pubs/CTProtocols/documents/AdultRoutineHeadCT.pdf. Accessed 10 Aug 2019
4. ACR–ASNR Practice Parameter for the Performance of Computed Tomography (CT) of the Brain Revised 2015 (Resolution 20). https://www.acr.org/-/media/ACR/Files/Practice-Parameters/CT-Brain.pdf. Accessed 10 Aug 2019
5. Sodickson A, Okanobo H, Ledbetter S. Spiral head CT in the evaluation of acute intracranial pathology: a pictorial essay. Emerg Radiol. 2011 Jan; 18(1): 81-91.
6. Kim ES, Yoon DY, Lee H et al. Comparison of emergency cranial CT

interpretation between radiology residents and neuroradiologists: transverse versus three dimensional images. Diagn Interv Radiol. May-Jun 2014; 20(3): 277-284.

7. Zacharia TT, Nguyen DT. Subtle pathology detection with multidetector row coronal and sagittal CT reformations in acute head trauma. Emerg Radiol. 2010 Mar; 17(2): 97-102.

8. Alberico RA, Loud P, Pollina J, Greco W, Patel M, Klufas R. Thick-section reformatting of thinly collimated helical CT for reduction of skull base-related artifacts. AJR Am J Roentgenol. 2000 Nov; 175(5): 1361-1366.

9. Takata T, Ichikawa K, Mitsui W, Hayashi H, Minehiro K, Sakuta K et al. Object shape dependency of in-plane resolution for iterative reconstruction of computed tomography. Phys Med. 2017 Jan; 33: 146-151.

10. Nickoloff EL. Measurement of the PSF for a CT scanner: appropriate wire diameter and pixel size. Phys Med Biol. 1988 Jan; 33(1): 149-155.

11. Ichikawa K, Kobayashi T, Sagawa M, Katagiri A, Uno Y, Nishioka R et al. A phantom study investigating the relationship between ground-glass opacity visibility and physical detectability index in low-dose chest computed tomography. J Appl Clin Med Phys. 2015 Jul 8; 16(4): 202-215.

12. Kleinman PL, Strauss KJ, Zurakowski D, Buckley KS, Taylor GA. Patient size

measured on CT images as a function of age at a tertiary care children's hospital. Am J Roentgenol. 2010 Jun; 194(6): 1611-1619.

13. Samei E, Richard S. Assessment of the dose reduction potential of a model-based iterative reconstruction algorithm using a task-based performance metrology. Med Phys. 2015 Jan; 42(1): 314-323.
14. Kawashima H, Ichikawa K, Matsubara K, Nagata H, Takata T, Kobayashi S (2019) Quality evaluation of image-based iterative reconstruction for CT: Comparison with hybrid iterative reconstruction. J Appl Clin Med Phys. 2019 Jun; 20(6): 199-205.
15. Ichikawa K, Kawashima H, Shimada M, Adachi T, Takata T. A three-dimensional cross-directional bilateral filter for edge-preserving noise reduction of low-dose computed tomography images. Comput Biol Med. 2019; 111: 103353 [Epub ahead of print]
16. Boedeker KL, Cooper VN, McNitt-Gray MF. Application of the noise power spectrum in modern diagnostic MDCT: part I. Measurement of noise power spectra and noise equivalent quanta. Phys Med Biol. 2007 Jul 21; 52(14): 4027-4046.
17. International Commission on Radiation Units and Measurements; 1996. Medical imaging—the assessment of image quality. ICRU report No. 54, ICRU Publications, Bethesda.

18. Hsieh J; 2009. Slice-sensitivity profile and noise In: Jiang Hsieh (ed) Computed tomography: principles, design, artifacts, and recent advances, 2nd edn. SPIE Press, Bellingham, WA, pp 348-354

19. Lin XZ, Miao F, Li JY, et al. High-definition CT Gemstone spectral imaging of the brain: initial results of selecting optimal monochromatic image for beam-hardening artifacts and image noise reduction. J Comput Assist Tomogr. Mar-Apr 2011; 35(2): 294-297.

20. Mackenzie A, Honey ID. Characterization of noise sources for two generations of computed radiography systems using powder and crystalline photostimulable phosphors. Med Phys. 2007 Aug; 34(8): 3345–3357.

21. Samei E; 2019. Performance evaluation of computed tomography systems: Report of AAPM Task Group 233, American Association of Physicists in Medicine.

22. Ichikawa K, Hara T, Urikura A, Takata T, Ohashi K. Assessment of temporal resolution of multi-detector row computed tomography in helical acquisition mode using the impulse method. Phys Med. 2015 Jun; 31(4): 374–381.

Biography

1) Fujimura I, Ichikawa K, Miura Y, Hoshino T, Terakawa S. Comparison of physical image qualities and artifact indices for head computed tomography in the axial and helical scan modes. Phys Eng Sci Med. 2020 Jun; 43 (2): 557-566.

2) 宮安孝行，藤村一郎，鈴木淳平，小倉圭史，田代雅実，田中善啓，大保勇，赤木憲明，五十嵐隆元，坂下惠治．外傷全身 CT 撮影における被ばく線量（CTDIvol と DLP）の国内実態調査．日本臨床救急医学会雑誌．2019；22：715-722.

3) Nakao S, Ishikawa K, Ono H, Kusakabe K, Fujimura I, Ueno M, Idoguchi K, Mizushima Y, Matsuoka T. Radiological classification of retroperitoneal hematoma resulting from lumbar vertebral fracture. Eur J Trauma Surg. 2019 Apr; 45 (2): 353-363.

4) Miura Y, Ichikawa K, Fujimura I, Hara T, Hoshino T, Niwa S, Funahashi M. Comparative evaluation of image quality among different detector configurations using area detector computed tomography. Radiological Physics and Technology. 2018 Mar; 11(1): 54-60, 2018.

5) 藤村一郎，西池成章，相良健司，安永桂介，長谷川勝俊，坂下惠治．バックボード固定下頭部 CT 撮影におけるポジショニング位置が画質に及ぼす影響.

JSCT_Proceediongs 2015.

6) 星野貴志，市川勝弘，寺川彰一，勝眞康行，藤村一郎，上田祐二，三浦洋平，西村健司. 逐次近似再構成法が三次元 CT 画像の形状再現性に与える影響. 日本放射線技術学会雑誌. 2012；68（12）: 1624-1630.

7) 藤村一郎，西池成章，相良健司，坂下惠冶，松岡哲也．外傷パンスキャンの被ばくと画質に関する検討. 日本臨床救急医学会雑誌. 2012 ; 15（5）: 617-624.

8) 三浦洋平，市川勝弘，原　孝則，丹羽伸次，藤村一郎，寺川彰一．低線量胸部 CT 画像における低コントラスト分解能の評価. 日本放射線技術学会雑誌. 2011　；67（8）: 873-879.

9) 藤村一郎，市川勝弘，寺川彰一，原　孝則，三浦洋平．頭部 CT におけるヘリカルスキャンとノンヘリカルスキャンのモーションアーチファクトに関する検討．日本放射線技術学会雑誌．2011；67(6)：640-647.

10) Mizobata Y, Yokota J, Fujimura I, Sakashita K. Successful evaluation of pseudoaneurysm formation after blunt renal injury With dual-phase contrast-enhanced helical CT. AJR Am J Roentgenol. 2001 Jul;　177(1): 136-138.